Biomimetic design of ultrathin edge-riched FeOOH@Carbon nanotubes as high-efficiency electrocatalysts for water splitting

Huanxin Li[a,1], Qiang Zhou[a,1], Fuyu Liu[a], Wenlong Zhang[a], Zhong Tan[a], Haihui Zhou[a,*], Zhongyuan Huang[a,*], Shuqiang Jiao[b,*], Yafei Kuang[a,*]

[a] State Key Laboratory for Chemo/Biosensing and Chemometrics, College of Chemistry and Chemical Engineering, Hunan University, Changsha, Hunan, 410082, China
[b] State Key Laboratory of Advanced Metallurgy, University of Science and Technology Beijing, Beijing, 100083, China

ARTICLE INFO

ABSTRACT

Based on a plant-like morphology, here, we report a multidimensional composite with ultrathin edge-riched FeOOH "leaves" growing on carbon nanotube "branches" (FeOOH@CNTs) via a facile and environmentally benign approach. A Fenton reaction was adopted to oxidize carbon nanotubes (CNTs), and FeOOH flakes were generated on the CNTs as reaction proceeded. The highly conductive CNT "branches" ensure rapid electron transmission and compensate for low conductivity of the FeOOH "leaves". Meanwhile, ultrathin FeOOH "leaves" growing on CNT "branches" expose sufficient numbers of active sites for oxygen evolution reaction (OER). Density functional theory (DFT) computational results indicate that FeOOH@CNTs exhibit better OER catalytic performance than FeOOH. To achieve water splitting, FeOOH@CNTs were deposited on nickel foam as an anode, with platinum (Pt) sheet used as a cathode. A low cell voltage of only 1.44 V was achieved to yield a current density of 10 mA cm–2 with a TOF of 12.50 s-1.

1. Introduction

The cooperation of extensive leaves and branches in trees is one of the most efficient catalytic systems found in nature to convert solar energy into bioenergy through photosynthesis. In this "leaf-branch" system, leaves expose their maximum specific surface area to fully absorb solar energy for photosynthesis, with branches continuously delivering essential raw materials, such as water and nutrients. The synergy between branches and leaves in plant photosynthesis is a critical factor for maximizing photosynthetic efficiency, which is the result of a billion years of biological evolution. [1] Remarkably, the electrochemical catalytic process is very similar to the photosynthesis process observed in trees. In electrochemical catalysis, active sites accelerate the reaction rate, while current collectors are responsible for the rapid transmission of electrons. By imitating the "leaf-branch" system of trees and constructing catalytic "leaves" on highly conducting "branches", elevated catalytic performance should be achievable [2,3].

To this end, we have designed a "leaf-branch" catalyst for a specific electrocatalytic process, the oxygen evolution reaction (OER), which is critical to energy storage and conversion systems, such as water splitting, fuel cells and metal-air batteries. However, the high price of OER

catalysts has hindered the scalability of these systems. At present, the search for alternative OER catalysts to replace precious metal oxides (e.g. RuO_2 and IrO_2) is of keen interest. [4] Non-precious metals (Fe [5], Co [6], Ni [7], Mn [8] and Cu [9]) and their compounds were widely reported as potential candidates [10–13].

Among these, Fe-based catalysts, such as FeOOH, are particularly promising due to their intrinsic activity, low cost and environmentally benign nature. But the significant challenge for Fe hydroxide nanosheets is the poor electrical conductivity ($\tilde{}10^{-5}$ S cm^{-1}) that limits electrocatalytic performance. Li et al. presented a highly ordered FeOOH/Co/FeOOH hybrid and achieved superior catalytic activity and durability for OER [14]. Similarly, CNTs are highly conductive carbon materials which could overcome the poor electrical conductivity of FeOOH.

Taking inspiration from nature, a biomimetic design of "leaf-branch" morphology was achieved, in which the catalytic activity of FeOOH@CNTs for OER could be improved. The "leaf-like" FeOOH growing on CNTs could fully expose the active sites by minimizing their thickness, with CNTs constructing conductive "branches" to ensure adequate electron supply for the FeOOH "leaves". Thus, the FeOOH "leaves" and CNTs "branches" would fabricate an ordered and well-

connected "leaf-branch" morphology to achieve excellent catalytic activity and durability.

2. Experimental section

2.1. Catalyst preparation

All chemical reagents used were of analytical grade (AR) without any additional purification before use. First, 0.5 g carbon nanotubes (CNTs) and 5 g FeSO$_4$·7H$_2$O were placed in a beaker and mixed with 200 mL of ultra-pure water. 500 mL 30 wt. % H$_2$O$_2$ was then added gradually into the solution at 95 °C. Finally, the viscosity of the mixture significantly increased and the product was washed, centrifuged, and dried to obtain FeOOH@CNTs. As an extension of this method, FeOOH@graphite was also synthesized through the same approach (Fig. S1). As a comparison, FeOOH was prepared by the same method as FeOOH@CNTs, but without the addition of CNTs (see Fig. S2a).

Furthermore, for the synthesis of Ni$_x$Fe$_y$OOH@CNTs/NF, nickel foam (NF) was first washed by ethanol and HCl solution, then immersed into the CNTs/FeSO$_4$·7H$_2$O dispersion. Afterwards, H$_2$O$_2$ was added to initiate the Fenton reaction. When this reaction was complete, the mixture was dried at 60 °C to finally obtain the Ni$_x$Fe$_y$OOH@CNTs/NF.

2.2. Catalyst characterization

The catalysts were investigated using scanning electron microscopy (SEM, Histachi S-4800), transmission electron microscopy (TEM, JEOL JEM-2100 Plus) and a SmartLab XRD diffractometer with a Cu Kα source operating at 40 kV, 60 mA. X-ray photo-electron spectroscopy (XPS) analysis was performed on an ESCALAB250 XPS spectrometer with an Mg Ka X-ray source (1350 eV). The Brunauer Emmett Teller (BET) specific surface area was calculated based on physical nitrigen adsorption (Beckman Coulter SA-3100, USA). The concentration of elemental Fe in the composite was measured by inductively coupled plasma atomic emission spectrometry (ICPAES). The sample was measured at room temperature by an Isoacceleration-driven Mossbauer spectrometer (Wissel, Germany), with a ^{57}Co (Pd) radiation source, and the least square method was used to fit the spectrum. NH$_3$ temperature-programmed desorption (NH$_3$-TPD), H$_2$ temperature-programmed reduction (H$_2$-TPR) profiles, and CO-dispersion data were all obtained on an Automated chemisorption analyser (AutoChem II 2920).

2.3. Catalytic activity measurements

Electrochemical measurements were carried out on an electrochemical workstation (CHI 660E, CH instruments, Shanghai) using a conventional three-electrode set-up. Platinum plate was used as the counter electrode, saturated calomel electrode (SCE) acted as the reference, and glassy carbon was employed for coating samples as working electrodes. The preparation process of the working electrodes was as follows: 4 mg of product was dispersed in 2 mL deionized water and sonicated for 10 min, 25 μL suspension was then deposited onto the surface of the glassy carbon electrode and dried for 30 min. Afterwards, a further 5 μL of 0.5% Nafion solution (Sigma-Aldrich) was also deposited onto the electrode surface and dried for 10 min. The electrolyte used was 1 M KOH. All potentials were referenced to the reversible hydrogen electrode (RHE) via the following equation: E$_{(RHE)}$ = E$_{(SCE)}$ + 0.059*pH + 0.241 V. Linear sweep voltammetry (LSV) was measured at a scan rate of 5 mV s^{-1}. Prior to LSV testing, the electrodes were first subjected to 7 cycles of cyclic voltammetry (CV) in the range of 0 to 0.6 V (vs. SCE) at 50 mV s^{-1}, in order to stabilize the current. Tafel plots were then derived from the LSV data. Electrochemical impedance spectroscopy (EIS) was conducted at 1.23 V, with frequency ranging from 100 kHz to 0.01 Hz at an AC amplitude of 5 mV. The stability performance was measured at a given current density over a 10 h period. Turnover frequency (TOF) values for the catalysts were
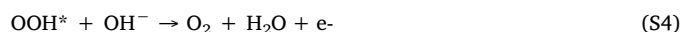
calculated from the equation: TOF = j*A/(4*F*m).

j is the current density, A is the area of the electrode, F is the Faraday constant (96,485 C mol^{-1}), m is the number of moles of active material that is deposited onto the electrode, which is estimated by the equation:

m = m$_{(FeOOH@CNTs)}$*ω$_{(Fe\ in\ FeOOH@CNTs)}$/ω$_{(Fe\ in\ FeOOH)}$. ω is the mass fraction of Fe.

2.4. Computational modelling

The spin-polarized density functional theory (DFT) calculations were performed using the Vienna Ab initio Simulation Package (VASP). [15,16], DFT + U formalism was used to calculate free energies, electron-ion interactions with GGA-PBE functional and an effective U-J value of 4.3 eV for Fe [17]. Projected augmented wave (PAW) potentials were used to model electron-ion interactions, with a plane-wave cutoff energy of 300 eV. [18,19], Model structures of the FeOOH and FeOOH@CNTs layers were fully optimized, with the sampling k-point set to 3 × 3 × 1 grids. The convergence threshold was conducted at an energy of 10^{-4} eV and a force of 0.05 eV/Å. In an alkaline environment, the OER proceeds in four-electron step which can be written as follows:

$$* + OH^- \rightarrow OH* + e^- \tag{S1}$$

$$OH* + OH^- \rightarrow O* + H_2O + e^- \tag{S2}$$

$$O* + OH^- \rightarrow OOH* + e^- \tag{S3}$$

$$OOH* + OH^- \rightarrow O_2 + H_2O + e- \tag{S4}$$

Where * represents an adsorption site on the catalyst, and OH*, O* and OOH* denote the corresponding adsorbed intermediates. Also, at standard conditions, the free energies change for all OER electrochemical steps (ΔG$_{1-4}$) can be expressed as:

$$\triangle G_1 = \triangle G_{OH*} \tag{S5}$$

$$\triangle G_2 = \triangle G_{O*} - \triangle G_{OH*} \tag{S6}$$

$$\triangle G_3 = \triangle G_{OOH*} - \triangle G_{O*} \tag{S7}$$

$$\triangle G_4 = 4.92 - \triangle G_{OOH*} \tag{S8}$$

Therefore, the theoretical overpotential η is defined as the equation: η$_{theory}$ = max{$\triangle G_1$, $\triangle G_2$, $\triangle G_3$, $\triangle G_4$}/e–1.23 V (S9), the reaction free energy for adsorbate ($\triangle G_{ads}$) was calculated according to the following formula: $\triangle G_{ads}$ = $\triangle E_{ads}$ + $\triangle E_{ZPE}$ – T$\triangle$S (S10)

Where E$_{ZPE}$ is the zero energy, $\triangle$S is the entropy change, and T is the system temperature (298.15 K, in our work). The E$_{ZPE}$ and T$\triangle$S values calculated for each gas-phase species and adsorbate are listed in Tab.S2. Moreover, the aforementioned binding energies ($\triangle E_{ads}$) for OOH*, O* and OH* could be calculated by the following equations:

$$\triangle E_{OOH*} = E_{OOH*} - E_* - (2E_{H2O} - 3/2E_{H2}) \tag{S11}$$

$$\triangle E_{O*} = E_{O*} - E_* - (E_{H2O} - E_{H2}) \tag{S12}$$

$$\triangle E_{OH*} = E_{OH*} - E_* - (E_{H2O} - 1/2E_{H2}) \tag{S13}$$

Where E$_*$, E$_{OOH*}$, E$_{O*}$ and E$_{OH*}$ represent the total energy values calculated by DFT for the pristine substrate and those adsorbed with OOH*, O* and OH*, respectively. In addition, E$_{H2O}$ and E$_{H2}$ are the total respective energies of the H$_2$O and H$_2$ molecules in the gas phase.

3. Results and discussion

3.1. Synthesis of "leaf-branch" structural FeOOH@CNTs

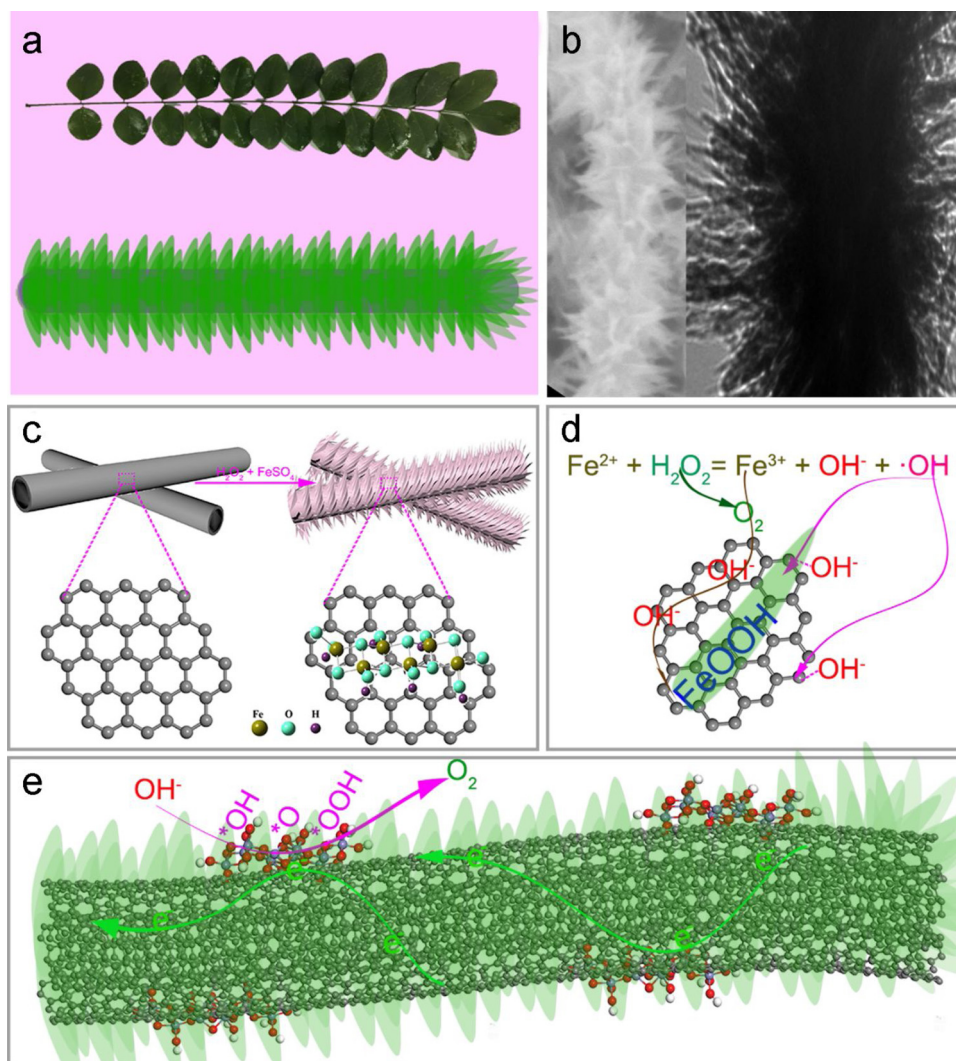Inspired by the cooperation of plant branches and leaves during

Fig. 1. (a) Model of a leaf-branch structure; (b) Electrocatalyst with a leaf-branch structure; (c) The leaf-branch synthesis process and (d) Reaction mechanism of the electrocatalyst; (e) Schematic of FeOOH@CNTs electrocatalysis process.

photosynthesis, we have proposed a similar structural design for an oxygen evolution catalyst. Images of an individual branch and the corresponding structure of an ideal "leaf-branch" electrocatalyst are presented in Fig. 1**a**. According to this concept, we constructed a FeOOH@CNTs composite with ultrathin edge-riched FeOOH "leaves" supported by carbon nanotube "branches" as an OER catalyst. A facile one-step Fenton reaction was employed to synthesize the FeOOH@CNTs composite with an ordered "leaf-branch" structure (Fig. 1b). The synthesis process was followed as presented in Fig. 1**c**. CNTs were well dispersed in ultra-pure water, and then mixed with H_2O_2 and $FeSO_4$ solutions. Fe^{2+} rapidly reacts with H_2O_2 to produce OH^- and $\cdot OH$ radicals, while Fe^{2+} is oxidized to Fe^{3+}. The $\cdot OH$ radicals attack CNTs, thus forming plentiful defects and oxygen-containing functional groups on which the Fe^{3+} can adsorb and convert into FeOOH using surrounding OH^- and O_2 (Fig. 1d). Eventually, the final structure of numerous ordered FeOOH "leaves" growing on CNT "branches" was achieved. To verify this reaction mechanism and the success of this strategy, graphite powders were also treated to the same Fenton reaction process. Consequently, the graphite powders were oxidized into graphitic spheres, onto which FeOOH flakes were generated and deposited (FeOOH@graphite, see Fig. S1). Therefore, we believe that $\cdot OH$ radicals produced during the Fenton reaction could oxidize graphitic carbon, and the FeOOH flakes could be formed on their surface. In addition, "leaf-branch" structural FeOOH@CNTs could

be an ideal structure for OER catalysts. During the catalytic process, as shown in Fig. 1e, internal CNT "branches" are supplied with electron transmission channels, while external ultrathin edge-riched FeOOH "leaves" provide plentiful catalytic sites.

3.2. Catalyst characterization and analysis

The morphology and composition of the FeOOH@CNTs composite was investigated. SEM images of FeOOH@CNTs at different magnifications are shown in Fig. 2a, **b**, which demonstrate that high numbers of ordered "leaves" grew on the cross-linked CNT "branches". The diameter of the "branches" is ˜100 nm and the "leaves" are ˜50 nm in length. Fig. 2c, **d** are TEM images of FeOOH@CNTs, also demonstrating that the "leaves" are uniformly distributed on the CNT "branches". The HRTEM image of FeOOH@CNTs shown in Fig. 2**e** demonstrates that the lattice stripes (0.245 nm) of the "leaves" are corresponded to the (111) plane of FeOOH. Typical TEM and corresponding mapping images of FeOOH@CNTs are illustrated in Fig. 2**f-i**, in which elemental C is shown to mainly concentrate on the CNT "branches" and Fe and O are evenly distributed on both the "branches" and "leaves". To further reveal the structure and composition of the FeOOH@CNTs composite, XRD and XPS analyses were performed and the results are shown in Fig. 2**j-l**. The XRD pattern in Fig. 2j demonstrates four dominant peaks at $2\theta = 21.22°$, $36.65°$, $39.98°$ and $53.24°$, corresponding to the(110),
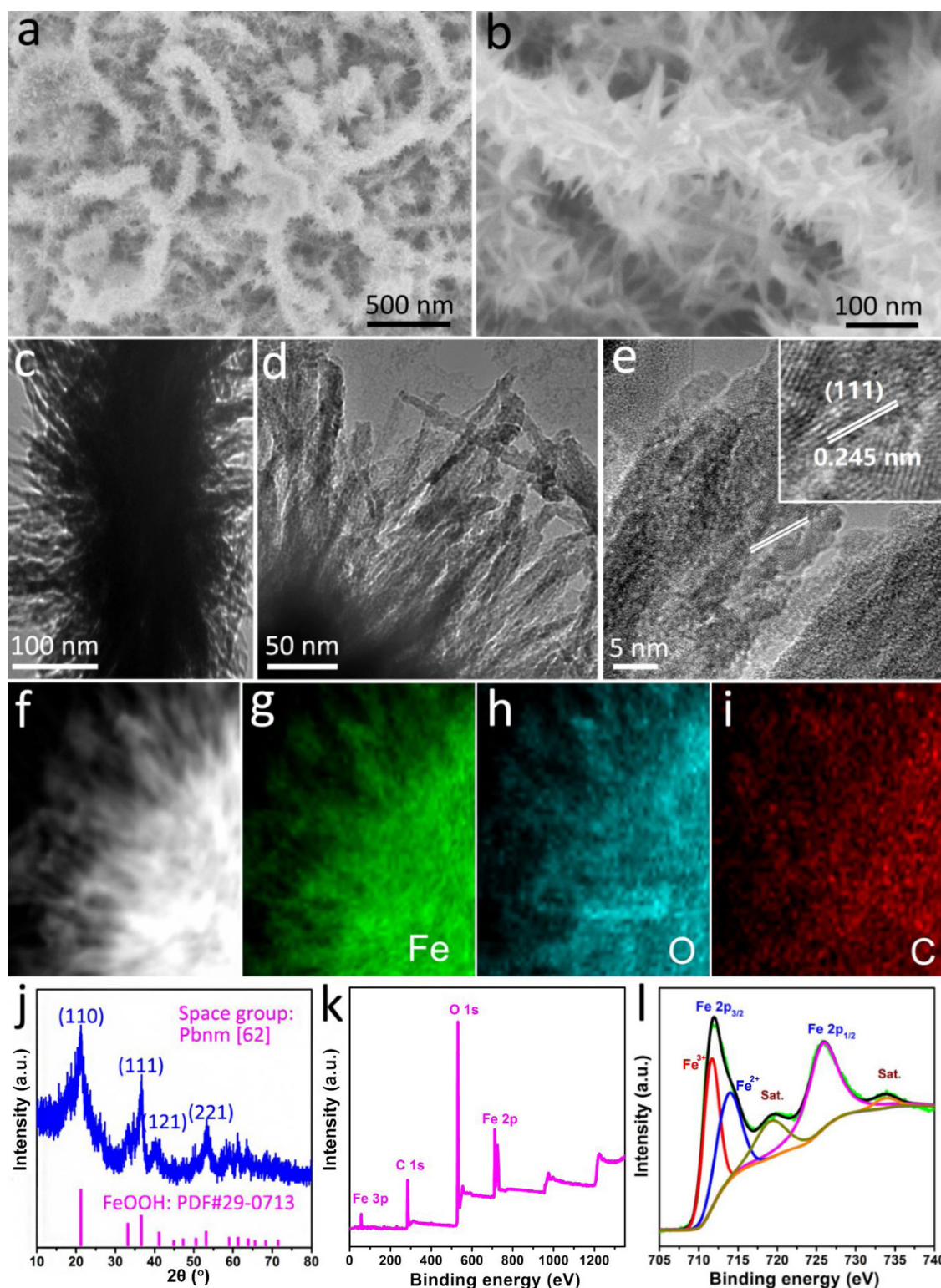
Fig. 2. (a, b) SEM images of FeOOH@CNTs; (c, d) TEM images of FeOOH@CNTs; (e) HRTEM image of FeOOH@CNTs; (f–i) TEM image of FeOOH@CNTs and corresponding EDS mapping images of Fe, O and C; (j) XRD pattern of FeOOH@CNTs; (k) XPS spectrum of FeOOH@CNTs; (l) High-resolution XPS spectra of Fe 2p in FeOOH@CNTs.

(111), (121) and (221) of FeOOH, respectively (PDF#29-0713, space group: Pbnm [62]), indicating the existence of FeOOH in the composite (For detailed XRD patterns of FeOOH@CNTs and pure FeOOH see Fig. S4). The XPS survey of FeOOH@CNTs is shown in Fig. 2k, which demonstrates dominant peaks for Fe 3p, C 1s, O 1s and Fe 2p at binding energies of 55.8, 284.6, 531.8 and 711.9 eV. The mass ratios of C, O and Fe elements are 33.7, 49.0 and 17.3 at. %, respectively. The high-resolution XPS spectrum of Fe 2p for FeOOH@CNTs shows typical characteristic peaks of FeOOH, with two main peaks located at 711.9 and 726.0 eV, further proving the existence of FeOOH in the composite (Fig. 2l). [8]

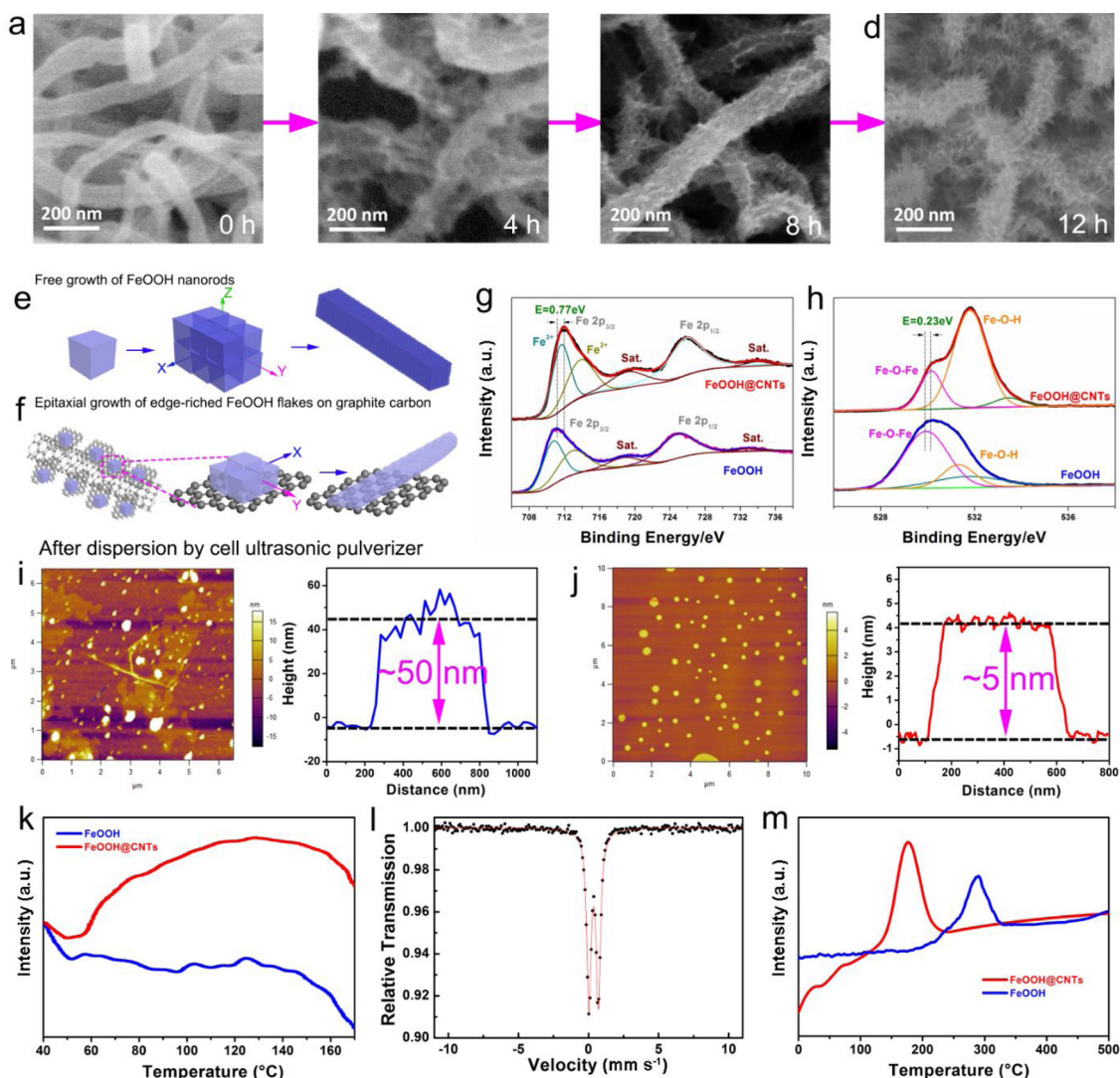To investigate the possible interactions that occur with CNTs during

Fig. 3. (a–d) SEM images of FeOOH@CNTs at reaction time of 0, 4, 8, 12 h; (e, f) Growth mechanism of FeOOH and FeOOH@CNTs; (g) XPS spectra of Fe 2p in FeOOH@CNTs and FeOOH; (h) XPS spectra of O 1s in FeOOH@CNTs and FeOOH; (i) AFM images and corresponding thickness analysis of FeOOH and (j) FeOOH@CNTs after dispersion by cell ultrasonic pulverizer; (k) NH$_3$-TPD profiles of FeOOH and FeOOH@CNTs; (l) Mossbauer spectrum of Fein FeOOH@CNTs;(m) H$_2$-TPR profiles of FeOOH and FeOOH@CNTs.

the Fenton reaction, SEM images of product materials after different reaction time are shown in Fig. 3**a-d**. The surface of original CNTs sample is relatively smooth (Fig. 3b), however, many folds appear on the surface as the Fenton reaction proceeds (Fig. 3b), indicating oxidation. The rough surface of the CNT "branches" should be conducive to forming a tight connection to the FeOOH "leaves". Afterwards, FeOOH "leaves" start to grow on the surface of the CNT "branches" (Fig. 3c, **d**). As observed, the FeOOH "leaves" are thinner than the pure FeOOH shown in the SEM images (Fig. S2). We deduce that the growth mechanism of FeOOH@CNTs tends to an epitaxial mode based on the surface of the carbon flakes (Fig. 3f), whilst pure FeOOH grows freely in three dimensions (Fig. 3e). Since CNTs would be attacked by ·OH radicals during the Fenton reaction, large quantities of defects and small vertical carbon nanosheets can be formed on the CNT surface (Fig. 3f). Fe^{3+} ions were preferentially adsorbed onto defect sites which then generated FeOOH nanoflakes along the length of the vertical carbon nanosheets through an epitaxial growth strategy. This finally led to the formation of the FeOOH@CNTs, with the FeOOH nanoflakes growing almost vertically onto the CNTs. Just as a close interconnection and adequate raw material transfer is required between the branches and leaves of a tree for efficient photosynthesis, an effective interconnection

and rapid electron transfer between the "leaves" and "branches" in electrocatalysts is necessary to ensure excellent catalytic performance. To further verify the electronic interactions between FeOOH "leaves" and CNT "branches", XPS spectra of Fe 2p in FeOOH@CNTs and FeOOH were obtained, as shown in Fig. 3**g** [20]. Pure FeOOH demonstrates two main peaks of Fe 2p at 711.17 and 725.23 eV, while the Fe 2p3/2 and 2p1/2 peaks in FeOOH@CNTs shift to 711.94 and 726.0 eV, respectively. The positive shifts (ca. 0.77 eV) of the Fe peaks in binding energy reveal the electron interactions existing between the FeOOH "leaves" and CNT "branches" within the FeOOH@CNTs [21]. Moreover, XPS spectra for O 1s in FeOOH@CNTs are shown in Fig. 3**h**. The electron interactions between FeOOH "leaves" and CNT "branches" in FeOOH@CNTs were also reflected by a positive shift (0.23 eV) of O 1s peaks in FeOOH@CNTs compared to that of pure FeOOH. In addition, the O 1s peaks can be assigned to Fe-O-H (~535.1 eV) and Fe-O-Fe bonds (~532.0). It can be rationally argued that the Fe-O-H bonds come from the surface of the FeOOH "leaves", while Fe-O-Fe bonds exist in the bulk. From Fig. 3**h** we observed that the ratio of Fe-O-H to Fe-O-Fe in FeOOH@CNTs is 3.42, which is greater than that in pure FeOOH (0.31). This indicates that the ultrathin edge-riched FeOOH "leaves" on the CNT "branches" have a greater exposed surface area. Moreover, cyclic

voltammetry measurements of FeOOH and FeOOH@CNTs measured in alkaline solution (Fig. S5a) also reveal that the FeOOH "leaves" on the CNT "branches" possess a larger surface area than that of pure bulk FeOOH. To verify this, FeOOH and FeOOH@CNTs were first dispersed by a cell ultrasonic pulverizer, in order to obtain a few individual FeOOH flakes from the composite. During pulverization these flakes partially detached and became more rounded in shape (Fig. 3j). AFM analysis of FeOOH and FeOOH@CNTs after dispersion are shown in Fig. 3i and j. This demonstrates that the thickness of FeOOH (~50 nm) is almost 10 times that of the FeOOH "leaves" (~5 nm) in FeOOH@CNTs, indicating there are more exposed surface in FeOOH@CNTs. Meanwhile, NH_3-TPD profiles of FeOOH and FeOOH@CNTs (Fig. 3k) demonstrate that FeOOH@CNTs exhibit a much larger adsorption capacity than FeOOH, implying that more adsorption sites are present on the FeOOH@CNTs surface. Moreover, the Mossbauer spectrum (Fig. 3l) of Fe in FeOOH@CNTs exhibits only a quadrupole-split center line, without an observed Zeeman line. This indicates that the size of Fe-species in the composite is sufficiently small enough to induce super-paramagnitic behaviour. [22] The CO-dispersion test of FeOOH@CNTs further reveals the average particle diameter of Fe-species in the composite to be only 9.46 nm. The H_2-TPR profile of FeOOH@CNTs shown in Fig. 3m demonstrates that the reduction behaviour of FeOOH@CNTs occurs at ~185 °C, which is much lower than that of FeOOH (~290 °C) and those values reported in literature(250–450 °C) [23,24] As a result, FeOOH@CNTs catalysts should possess high effective surface areas and accordingly will display enhanced electrocatalytic activity.

3.3. Catalytic performance

The catalytic performances of FeOOH@CNTs, pure FeOOH and RuO_2 were studied using a standard three-electrode system in 1 M KOH. [25] From the polarization curves in Fig. 4a, we observe that the onset potential of FeOOH@CNTs is much lower, and the current density is much higher than that of FeOOH and RuO_2. Specifically, the FeOOH@CNTs only requires 206 mV of overpotential to reach a current density of 10 mA cm^{-2}, which is much lower than that of FeOOH powder (over 441 mV) and pure RuO_2 (259 mV). The above results indicate that the FeOOH@CNTs catalyst has excellent electrocatalytic activity in alkaline solution. [26] Remarkably, even when the current density reaches 50 mA cm^{-2}, the overpotential is still only 267 mV. This is one of the best results for FeOOH-based catalysts and other non-precious metal catalysts for OER in alkaline media (Table S3).

In the Tafel diagram (Fig. 4b), compared with FeOOH (168 mV dec^{-1}) and RuO_2 (111 mV dec^{-1}), the Tafel slope (31 mV dec^{-1}) of FeOOH@CNTs is much smaller, indicating a possible change in the control step. To investigate the electron transfer kinetics occurring at the electrode/electrolyte interface, electrochemical impedance spectroscopy (EIS) tests were performed in 1 M KOH (Fig. 4c). As shown, the semicircle diameter for FeOOH@CNTs is much smaller than that for FeOOH, which indicates that the FeOOH@CNTs catalyst possesses a faster electron transfer rate and lower electronic resistance. The electrical conductivity measured with a four probe method demonstrates the conductivities for FeOOH and FeOOH@CNTs composite were ~1.6×10^{-6} S cm^{-1} and ~2.3 S cm^{-1}, respectively, which is also consistent with previous literature [27]. These results indicate that the "leaf-branch" structure enhances electron transfer in FeOOH@CNTs.

In addition to the high OER catalytic activity, stability is another important factor for evaluating the quality of electrocatalysts. The stability tests of FeOOH and FeOOH@CNTs that were initiated at overpotential of 0.35 V are shown in Fig. 4d. Here the current density of
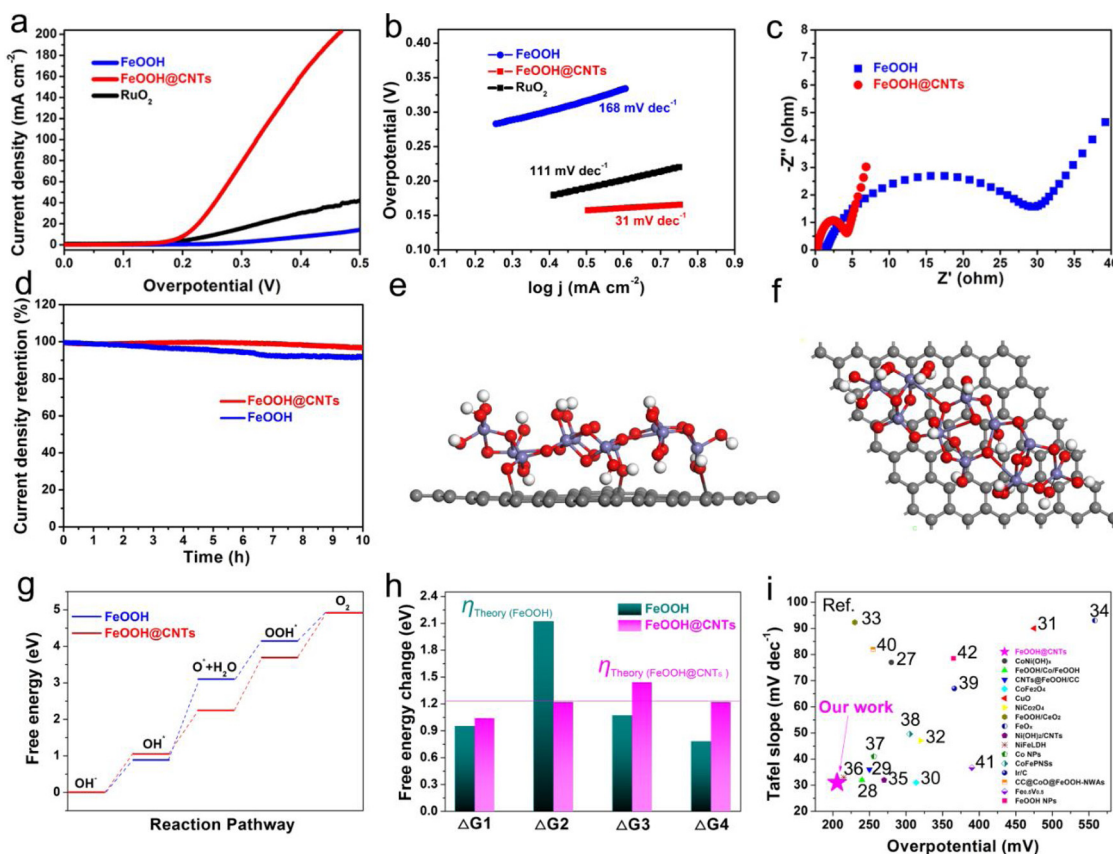

Fig. 4. (a) Polarization curves of RuO_2, FeOOH and FeOOH@CNTs for OER at a scan rate of 10 mV s^{-1}; (b) Tafel plots of RuO_2, FeOOH and FeOOH@CNTs; (c) Nyquist plots of FeOOH and FeOOH@CNTs; (d) Current density retentions of FeOOH and FeOOH@CNTs at overpotential of 0.35 V; (e) Front view and (f) top view of a theoretically optimized structure of FeOOH@CNTs; (g) Free energy profiles of FeOOH and FeOOH@CNTs; (h) Free energy changes of FeOOH and FeOOH@CNTs; (i) Comparison of overpotential (at a current density of 10 mA cm^{-2}) and Tafel slope of FeOOH@CNTs with those of other reported OER catalysts.

FeOOH@CNTs shows negligible degradation after 10 h, while the curve for FeOOH demonstrates a distinct attenuation, indicating that FeOOH@CNTs catalysts possess better stability during OER. Moreover, the faradaic efficiency of FeOOH@CNTs for OER is calculated to be ~99.54% (Fig. S7), making it a promising candidate for future energy conversion systems.

DFT calculations also reveal that the synergistic effects of FeOOH "leaves" and CNT "branches" could help to reduce the energy barrier for OER. Fig. 4e, f are the front and top views of the theoretically optimized structural model of FeOOH@CNTs. Here we can observe that the CNT "branches" are well bonded to the FeOOH "leaves", which is consistent with XPS data. Spin-polarized density functional theory computations were then carried out to better investigate the potential mechanisms for improving the OER catalytic activity of FeOOH@CNTs (see support information for calculation details Table S1, S2). Initially, the adsorption energies of the OER intermediates (O*, OH and OOH*) and the free energies of the four basic steps of FeOOH (ΔG_n, n = 1–4) were calculated. [28] As shown in Fig. 4g, h, the controlling step of the catalytic process of FeOOH in OER is the conversion process of OH* to O*, which has a ΔG_2 of 2.12 eV ($\Delta G_2 = \Delta G_{O*} - \Delta G_{OH*}$). It is known that the equilibrium potential of OER is 1.23 V and the overpotential of FeOOH is 0.89 V higher than the equilibrium potential, implying that the OER catalytic activity of FeOOH is relatively weak. On the contrary, the overpotential of FeOOH@CNTs is only 0.21 V higher than the equilibrium potential, which implies that the OER catalytic activity of FeOOH@CNTs is excellent. Therefore, the "leaf-branch" structure of FeOOH@CNTs can reduce the energy barriers of intermediates and products, thereby improving the overall electrocatalytic performance. It is an unexpected result that the CNT in FeOOH@CNTs can also stabilize the reaction intermediate according to the DFT calculation results, which might be due to the p, π-conjugation effect of C atoms in graphene and O atoms in FeOOH reduces the density of electron clouds around the central Fe atoms and enhances the adsorption ability of central Fe atoms, resulting in a more stable reaction intermediate. Compared to other nonprecious metal-based catalysts, the FeOOH@CNTs catalyst exhibits the lowest overpotential and Tafel slope (Fig. 4i). [29–44] From the above results, we ascribe the impressive electro-catalytic performance of the FeOOH@CNTs catalyst to the three aspects: a. The tight connection between CNT "branches" and FeOOH "leaves" alters the electronic cloud density around active sites, reducing the energy barrier of the intrinsic reaction; b. The CNT "branches" ensure rapid electron transfer during the catalytic process to improve reaction kinetics; c. The FeOOH "leaves" with numerous active sites thoroughly and uniformly disperse onto the CNT "branches".

To briefly investigate the possibility for practical applications, FeOOH@CNTs catalysts were loaded onto nickel foam [45] ($Ni_xFe_yOOH@CNTs/NF$) as shown in **Figure S8** (for synthesis see Supporting Information). Furthermore, $Ni_xFe_yOOH@CNTs/NF$ was used as an anode and platinum (Pt) sheet [46–48] as a cathode for overall water splitting. A cell voltage of only 1.44 V was required to achieve a current density of 10 mA cm^{-2} (Fig. 5a, it is worth mentioning that nickel foam has a three-dimensional architecture but the current density here was normalized only by two-dimensional geometric area), which is much lower than that achieved with a pure NF anode (1.63 V). In fact, the OER catalytic activity of $Ni_xFe_yOOH@CNTs/NF$ compares favourably with many other state-of-the-art catalysts on NF (Fig. 5b). [49–57] XPS analysis of $Ni_xFe_yOOH@CNTs/NF$ (Fig. S9) indicates that elemental Ni [58] is successfully doped into FeOOH@CNTs from NF, in the form of both Ni^0 and Ni-O-H. [59,60], The doped Ni content in $Ni_xFe_yOOH@CNTs$ is estimated to be ~3.6 at.% by XPS (Fig. S9a) and 6.92 wt.% by ICP-AES analysis, which should be conducive to improving OER performances since NiFe LDH are generally regarded as the most active OER catalysts in alkaline conditions. [61,62], We suggest that Ni could be doped into FeOOH because the ˙OH radicals formed during Fenton reaction would attack the Ni foam, which might generate Ni^{2+} ions and then diffuse into FeOOH@CNTs.

Fig. 5 (a) Cell voltage for water splitting of NF and $Ni_xFe_yOOH@CNTs/NF$; (b) Comparison of overpotentials (at a current density of 100 mA cm^{-2}) and Tafel slope of $Ni_xFe_yOOH@CNTs/NF$ with other reported OER catalysts

3.4. Discussion of the "leaf-branch" structure role

In nature, the "leaf-branch" system for trees is the most efficient for photosynthesis. Branches are responsible for the rapid and timely delivery of water and nutrients to the leaves for this photosynthesis, while leaves, with large specific surfaces, not only provide a location for photosynthesis, but also collect as much sunlight as possible for photocatalysis.

Similarly, an efficient electrocatalytic process can be achieved by biomimetic design of FeOOH and carbon nanotubes with characteristics of this "leaf-branch" structure. "Leaf-branch" structural FeOOH@CNTs was realized through a Fenton reaction, during which CNT "branches" were first oxidized and formed into small carbon flakes on the surface. The FeOOH "leaves" tended to an epitaxial growth along the carbon flakes, forming unique "leaf-branch" structures of FeOOH@CNTs. Carbon nanotubes, with a diameter of about 50 nm, connected to numerous FeOOH nanoflakes. It is the carbon nanotubes, with excellent electrical conductivity, that are responsible for the rapid and timely transmission of electrons generated during the reaction to an external circuit. FeOOH has a large specific surface area which offers a reaction residence for OER. This provides high numbers of active catalyst centers, and also ensures the desired electron transformation during the reaction process, due to a close connection with the carbon nanotubes. The rational structural design can maximize the catalytic activity. [63–66] Meanwhile, FeOOH also ensures that generated fine O_2 bubbles can leave the electrode surface in a timely manner, which greatly improves the oxygen evolution catalytic efficiency of FeOOH@CNTs. The combination and cooperation of FeOOH and carbon nanotubes promote the electrochemical oxidation of oxygen species, making the FeOOH@CNTs catalyst an appropriate option for OER.

Just as the "leaf-branch" system is the most efficient for photocatalysis in nature, the biomimetic design of "leaf-branch" structural FeOOH@CNTs can also realize state-of-the-art electrocatalysis. Table1 illustrates the TOF of catalysts with respect to metal contents, as reported in literature, with the inclusion of RuO_2. It suggests the FeOOH@CNTs catalysts used in our work achieves the highest value of TOF. The perfect synergism and combination of the FeOOH "leaves" and CNT "branches" in FeOOH@CNTs significantly improves the catalytic performance for OER [73,74].

4. Conclusion

In summary, we have proposed a "leaf-branch" strategy to design efficient OER electrocatalysts. FeOOH@CNTs structured with FeOOH "leaves" and CNT "branches" were fabricated via a facile Fenton reaction. During synthesis, CNT "branches" were attacked by hydroxyl radicals (˙OH), to form an excess of carbon folds and hydroxyl ions. FeOOH "leaves" were then generated on the surface to eventually completely cover these "branches". The FeOOH@CNTs catalyst has a unique "leaf-branch" structure, which ensures effective use of the FeOOH "leaves" during electrocatalytic reactions. Meanwhile, fast electron transfer was obtained by the CNT "branches", which plays a key role in improving the overall electrochemical performance. FeOOH@CNTs were also deposited onto nickel foam, to form FeOOH@CNTs/NF. This exhibited an overpotential of just 216 mV at 100 mA cm^{-2} and a Tafel slope of 26 mV dec^{-1} with a TOF of 12.50 s^{-1}. Remarkably, a total cell voltage of only 1.44 V was required to derive a current density of 10 mA cm^{-2} using a $Ni_xFe_yOOH@CNTs/NF$ anode and platinum (Pt) sheet cathode for overall water splitting. This is a competitive performance compared with reported OER catalysts. Our research provides a feasible and simple method to achieve an efficient
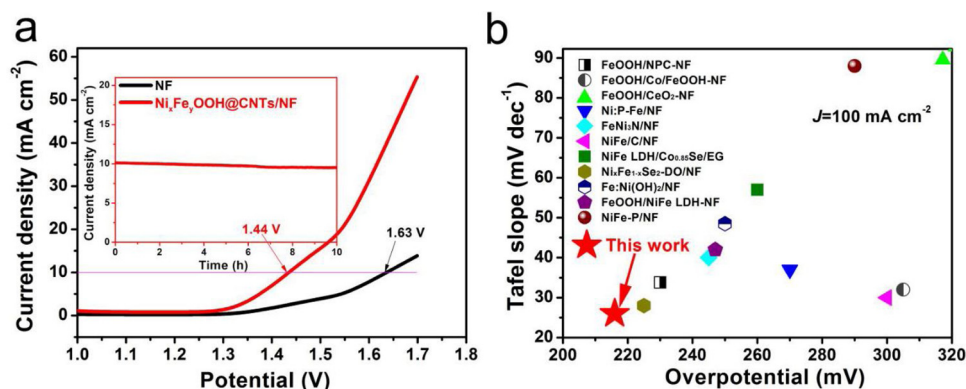
Fig. 5. (a) Cell voltage for water splitting of NF and Ni$_x$Fe$_y$OOH@CNTs/NF; (b) Comparison of overpotentials (at a current density of 100 mA cm^{-2}) and Tafel slope of Ni$_x$Fe$_y$OOH@CNTs/NF with other reported OER catalysts.

Table 1

Comparison of TOF value of the FeOOH@CNTs catalyst with that of other representative OER catalysts recently reported. (η_j: overpotential).

Catalyst	η_j /(mV)	TOF/(s^{-1})	Reference
FeOOH@CNTs	350	12.50	our work
FeOOH/Co/FeOOH HNTAs-NF	350	6.82	[14]
	400	10.15	
FeNi LDH-rGO	320	11.09	[67]
α-Ni(OH)$_2$ nanospheres	350	0.036	[68]
RuO$_2$	387	0.0104	[68]
20% Pt/C	387	0.0035	[68]
NG-CoSe$_2$	300	0.0356	[69]
CuO-NiO/NF	319	0.398	[70]
Co-Mo$_2$C NPs	350	0.108	[71]
Mo$_2$CT$_x$ NMs	200	0.0315	[72]

OER electrocatalyst, especially for weakly conducting metal oxides/hydroxides, and can also be expanded to design electrocatalysts with "leaf-branch" structures for abroad range of fields.

Appendix A. Supplementary data

Supplementary material related to this article can be found, in the online version, at doi:https://doi.org/10.1016/j.apcatb.2019.117755.

References

[1] L. Sack, C. Scoffoni, A.D. Mckown, K. Frole, M. Rawls, J.C. Havran, H. Tran, T. Tran, Developmentally based scaling of leaf venation architecture explains global ecological patterns, Nat. Commun. 3 (2012) 837.

[2] D.H. Xing, W.Y. Chen, Structural bionic design for high-speed machine tool working table based on distribution rules of leaf veins, Sci. China Technol. Sc. 55.8 (2012) 2091–2098.

[3] J.F. Ma, W.Y. Chen, L. Zhao, D.H. Zhao, Bionic design of columnar structure based on microstructure of bamboo, J. Mach. Des. 25.12 (2008) 50–53.

[4] T. Reier, M. Oezaslan, P. Strasser, Electrocatalytic oxygen evolution reaction (OER) on Ru, Ir, and Pt catalysts: a comparative study of nanoparticles and bulkmaterials, ACS Catal. 2.8 (2012) 1765–1772.

[5] T. Zhan, X. Liu, S.S. Lu, W. Hou, Nitrogen doped NiFe layered double hydroxide/reduced graphene oxide mesoporous nanosphere as an effective bifunctional electrocatalyst for oxygen reduction and evolution reactions, Appl. Catal. B Environ. 205 (2017) 551–558.

[6] S. Cai, Z. Meng, H. Tang, Y. Wang, P. Tsiakaras, 3D Co-N-doped hollow carbon spheres as excellent bifunctional electrocatalysts for oxygen reduction reaction and oxygen evolution reaction, Appl. Catal. B Environ. 217 (2017) 477–484.

[7] J.H. Kim, D.H. Youn, K. Kawashima, J. Lin, H. Lim, C.B. Mullins, An active nanoporous Ni(Fe) OER electrocatalyst via selective dissolution of Cd in alkaline media, Appl. Catal. B Environ. 225 (2018) 1–7.

[8] X. Zhao, X. Li, Y. Yan, Y. Xing, S. Lu, L. Zhao, S. Zhou, Z. Peng, J. Zeng, Electrical and structural engineering of cobalt selenide nanosheets by Mn modulation for efficient oxygen evolution, Appl. Catal. B Environ. 236 (2018) 569–575.

[9] B.K. Kim, S.K. Kim, S.K. Cho, J.J. Kim, Enhanced catalytic activity of electrodeposited Ni-Cu-P toward oxygen evolution reaction, Appl. Catal. B Environ. 237 (2018) 409–415.

[10] A. Pendashteh, J. Palma, M. Anderson, R. Marcilla, NiCoMnO$_4$ nanoparticles on N-doped graphene: highly efficient bifunctional electrocatalyst for oxygen reduction/evolution reactions, Appl. Catal. B Environ. 201 (2017) 241–252.

[11] R. Subbaraman, D. Tripkovic, K.C. Chang, D. Strmcnik, A.P. Paulikas, P. Hirunsit, M. Chan, J. Greeley, V. Stamenkovic, N.M. Markovic, Trends in activity for the water electrolyser reactions on 3d M (Ni, Co, Fe, Mn) hydr(oxy)oxidecatalysts, Nat. Mater. 11.6 (2012) 550.

[12] M. Jahan, Z. Liu, K.P. Loh, A Graphene oxide and copper-centered metal organic framework composite as a tri-functional catalyst for HER, OER, and ORR, Adv. Funct. Mater. 23.43 (2013) 5363–5372.

[13] X. Lu, C. Zhao, Electrodeposition of hierarchically structured three dimensional nickel–iron electrodes for efficient oxygen evolution at high current densities, Nat. Commun. 6 (2015) 6616.

[14] J.X. Feng, H. Xu, Y.T. Dong, S.H. Ye, Y.X. Tong, G.R. Li, FeOOH/Co/FeOOH hybrid nanotube arrays as high-performance electrocatalysts for the oxygen evolution reaction, Angew. Chem. 128.11 (2016) 3758–3762.

[15] G. Kresse, J. Hafner, Ab initio molecular dynamics for liquid metals, Phys. Rev. B 47 (1993) 558–561.

[16] G. Kresse, J. Furthmüller, Efficiency of ab-initio total energy calculations for metals and semiconductors using a plane-wave basis set, Comput. Mater. Sci. 6 (1996) 15–50.

[17] J.P. Perdew, K. Burke, M. Ernzerhof, Generalized gradient approximation made simple, Phys. Rev. Lett. 77 (1996) 3865.

[18] P.E. Blöchl, Projector augmented-wave method, Phys. Rev. B 50 (1994) 17953–17979.

[19] G. Kresse, D. Joubert, From ultrasoft pseudopotentials to the projector augmented-wave method, Phys. Rev. B 59 (1999) 1758–1775.

[20] A.L. Wang, X.J. He, X.F. Lu, H. Xu, Y.X. Tong, G.R. Li, Palladium– cobalt nanotube arrays supported on carbon fiber cloth as high performance flexible electrocatalysts for ethanol oxidation, Angew. Chemie Int. Edit. 54.12 (2015) 3669–3673.

[21] H. Abdel-Samad, P.R. Watson, An XPS study of the adsorption of lead on goethite (α-FeOOH), Appl. Surf. Sci. 136 (1998) 46–54.

[22] W. Kündig, H. Bömmel, G. Constabaris, R.H. Lindquist, Some properties of supported small α−Fe$_2$O$_3$ particles determined with the Mössbauer effect, Phys. Rev. 142.2 (1966) 327.

[23] A.E. Rahman, S.S. Ashour, H.M. Altass, K.S. Khairou, Pd nanoparticles supported on iron oxide nanorods for CO oxidation: effect of preparation method, J. Environ. Chem. Engin. 4.4 (2016) 4794–4800.

[24] B. Qiao, A. Wang, J. Lin, L. Li, D. Su, T. Zhang, Highly effective CuO/Fe(OH)$_x$ catalysts for selective oxidation of CO in H$_2$-rich stream, Appl. Catal. B Environ. 105 (2011) 103–110.

[25] T. Audichon, B. Guenot, S. Baranton, M. Cretin, C. Lamy, C. Coutanceau, Preparation and characterization of supported RuIr$_{(1-x)}$O$_2$ nano-oxides using a modified polyol synthesis assisted by microwave activation for energy storage applications, Appl. Catal. B Environ. 200 (2017) 493–502.

[26] S. Zhao, B. Rasimick, W. Mustain, H. Xu, Highly durable and active Co$_3$O$_4$ nanocrystals supported on carbon nanotubes as bifunctional electrocatalysts in alkaline media, Appl. Catal. B Environ. 203 (2017) 138–145.

[27] M.K. Choa, J.H. Jo, J.U. Choi, J. Kim, H. Yashiro, S. Yuan, L. Shi, Y.K. Sun,

S.T. Myung, Tunnel-type β-FeOOH cathode material for high rate sodium storage via a new conversion reaction, Nano Energy 41 (2017) 687–696.

[28] S. Zhao, Y. Wang, J. Dong, C.T. He, H. Yin, P. An, K. Zhao, X. Zhang, C. Gao, L. Zhang, J. Lv, J. Wang, J. Zhang, A.M. Khattak, N.A. Khan, Z. Wei, J. Zhang, S. Liu, H. Zhao, Z. Tang, Ultrathin metal–organic framework nanosheets for electro-catalytic oxygen evolution, Nat. Energy 1 (2016) 16184.

[29] C. Tang, H.S. Wang, H.F. Wang, Q. Zhang, G.L. Tian, J.Q. Nie, F. Wei, Spatially confined hybridization of nanometer-sized NiFe hydroxides into nitrogen-doped graphene frameworks leading to superior oxygen evolution reactivity, Adv. Mater. 27.30 (2015) 45164522.

[30] H. Liang, F. Meng, M. Cabán-Acevedo, L. Li, A. Forticaux, L. Xiu, Z. Wang, S. Jin, Hydrothermal continuous flow synthesis and exfoliation of NiCo layered double hydroxide nanosheets for enhanced oxygen evolution catalysis, Nano Lett. 15.2 (2015) 1421–1427.

[31] S. Klaus, Y. Cai, M.W. Louie, L. Trotochaud, A.T. Bell, Effects of Fe electrolyte impurities on Ni(OH)₂/NiOOH structure and oxygen evolution activity, J. Phys. Chem. C 119.13 (2015) 7243–7254.

[32] B.S. Yeo, A.T. Bell, Enhanced activity of gold-supported cobalt oxide for the electrochemical evolution of oxygen, J. Am. Chem. Soc. 133.14 (2011) 5587–5593.

[33] W. Luo, C. Jiang, Y. Li, S.A. Shevlin, X. Han, K. Qiu, Y. Cheng, Z. Guo, W. Huang, J. Tang, Highly crystallized α-FeOOH for a stable and efficient oxygen evolution reaction, J. Mater. Chem. A 5.5 (2017) 2021–2028.

[34] Y. Wang, Y. Ni, B. Liu, S. Shang, S. Yang, M. Cao, C. Hu, Vertically oriented CoO@ FeOOH nanowire arrays anchored on carbon cloth as a highly efficient electrode for oxygen evolution reaction, Electrochim. Acta 257 (2017) 356–363.

[35] J.X. Feng, S.H. Ye, H. Xu, Y.X. Tong, G.R. Li, Design and synthesis of FeOOH/CeO₂ heterolayered nanotube electrocatalysts for the oxygen evolution reaction, Adv. Mater. 28.23 (2016) 4698–4703.

[36] T.Y. Ma, S. Dai, M. Jaroniec, S.Z. Qiao, Graphitic carbon nitride nanosheet–carbon nanotube three-dimensional porous composites as high-performance oxygen evolution electrocatalysts, Angew. Chem. 126.28 (2014) 7409–7413.

[37] Y. Zhang, G. Jia, H. Wang, B. Ouyang, R.S. Rawat, H.J. Fan, Ultrathin CNTs@ FeOOH nanoflake core/shell networks as efficient electrocatalysts for the oxygen evolution reaction, Mater. Chem. Front. 1.4 (2017) 709715.

[38] K.Y. Yoon, H.J. Ahn, M.J. Kwak, S.I. Kim, J. Park, J.H. Jang, A selectively decorated Ti-FeOOH co-catalyst for a highly efficient porous hematite-based water splitting system, J. Mater. Chem. A 4.48 (2016) 18730–18736.

[39] K. Fan, Y. Ji, H. Zou, J. Zhang, B. Zhu, H. Chen, Q. Daniel, Y. Luo, J. Yu, L. Sun, Hollow Iron–vanadium composite spheres: a highly efficient iron-based water oxidation electrocatalyst without the need for nickel or cobalt, Angew. Chem. Int. Edit. 56.12 (2017) 3289–3293.

[40] T.M. Suzuki, T. Nonaka, K. Kitazumi, N. Takahashi, S. Kosaka, Y. Matsuoka, K. Sekizawa, A. Suda, T. Morikawa, Highly enhanced electrochemical water oxidation reaction over hyperfine β-FeOOH(Cl): Ni nanorod electrode by modification with amorphous Ni(OH)₂, Bull. Chem. Soc. Jpn. 91.5 (2018) 778–786.

[41] S. Li, Y. Wang, S. Peng, L. Zhang, A.M. Al-Enizi, H. Zhang, X. Sun, G. Zheng, Co–Ni-based nanotubes/nanosheets as efficient water splitting electrocatalysts, Adv. Energy Mater. 6.3 (2016) 1501661.

[42] Y. Liu, J. Li, F. Li, W. Li, H. Yang, X. Zhang, Y. Liu, J. Ma, A facile preparation of CoFe₂O₄ nanoparticles on polyaniline-functionalised carbon nanotubes as enhanced catalysts for the oxygen evolution reaction, J. Mater. Chem. A 4.12 (2016) 4472–4478.

[43] R. Chen, H.Y. Wang, J. Miao, H. Yang, B. Liu, A flexible high performance oxygen evolution electrode with three-dimensional NiCo₂O₄ core-shell nanowires, Nano Energy 11 (2015) 333–340.

[44] L. Wang, H. Chen, Q. Daniel, L. Duan, B. Philippe, Y. Yang, H. Rensmo, L. Sun, Promoting the water oxidation catalysis by synergistic interactions between Ni (OH)₂ and carbon nanotubes, Adv. Energy Mater. 6.15 (2016) 1600516.

[45] A. Sivanantham, S. Shanmugam, Nickel selenide supported on nickel foam as anEfficient and durable non-precious electrocatalyst for the alkaline water electrolysis, Appl. Catal. B Environ. 203 (2017) 485–493.

[46] M. Roca-Ayats, E. Herreros, G. García, M.A. Peña, M.V. Martínez-Huerta, Promotion of oxygen reduction and water oxidation at Pt-based electrocatalysts by titanium carbonitride, Appl. Catal. B Environ. 183 (2016) 53–60.

[47] S. Hu, G. Goenaga, C. Melton, T.A. Zawodzinski, D. Mukherjee, PtCo/CoO_x nano-composites: bifunctional electrocatalysts for oxygen reduction and evolution reactions synthesized via tandem laser ablation synthesis in solution-galvanic replacement reactions, Appl. Catal. B Environ. 182 (2016) 286–296.

[48] H. Wang, F.X. Yin, B.H. Chen, X.B. He, P.L. Lv, C.Y. Ye, D. Liu, ZIF-67 incorporated with carbon derived from pomelo peels: a highly efficient bifunctional catalyst for oxygen reduction/evolution reactions, Appl. Catal. B Environ. 205 (2017) 55–67.

[49] F. Li, J. Du, X. Li, J. Shen, Y. Wang, Y. Zhu, L. Sun, Integration of FeOOH and zeolitic imidazolate framework-derived nanoporous carbon as an efficient electrocatalyst for water oxidation, Adv. Energy Mater. 8.10 (2018) 1702598.

[50] Y. Li, C. Zhao, Iron-doped nickel phosphate as synergistic electrocatalyst for water oxidation, Chem. Mater. 28 (2016) 5659.

[51] B. Zhang, C. Xiao, S. Xie, J. Liang, Chen, Y. Tang, Iron–nickel nitride nanostructures in situ grown on surface-redox-Etching nickel foam: efficient and ultrasustainable electrocatalysts for overall water splitting, Chem. Mater. 28 (2016) 6934.

[52] Y. Feng, H. Zhang, L. Fang, Y. Mu, Y. Wang, Uniquely monodispersing NiFe alloyed nanoparticles in three-dimensional strongly linked sandwiched graphitized carbon sheets for high efficiency oxygen evolution reaction, ACS Catal. 6 (2016) 4477.

[53] Y. Hou, M.R. Lohe, J. Zhang, S. Liu, X. Zhuang, X. Feng, Vertically oriented cobalt Selenide/NiFe layered-double-Hydroxide nanosheets supported on exfoliated graphene foil: an efficient 3D electrode for overall water splitting, Energy Environ. Sci. 9 (2015) 478–483.

[54] X. Xu, F. Song, X. Hu, A nickel iron diselenide-derived efficient oxygen-evolution catalyst, Nat. Commun. 7 (2016) 12324.

[55] W. Zhang, J. Qi, K. Liu, R. Cao, A nickel-based integrated electrode from an autologous growth strategy for highly efficient water oxidation, Adv. Energy Mater. 6 (2016) 1502489.

[56] S. Dutta, A. Indra, Y. Feng, T. Song, U. Paik, Self-supported nickel iron layered double hydroxide-nickel selenide electrocatalyst for superior water splitting activity, ACS Appl. Mater. Interface 9 (2017) 33766.

[57] J. Xing, H. Li, M.C. Cheng, S. Geyer, K.Y.S. Ng, Electro-synthesis of 3D porous hierarchical Ni-Fe phosphate film/Ni foam as high-efficiency bifunctional electrocatalyst for overall water splitting, J. Mater. Chem. A 4 (2016) 13866.

[58] J. Chang, Q. Lv, G. Li, J. Ge, C. Liu, W. Xing, Core-shell structured Ni₁₂P₅/Ni₃(PO₄)₂ hollow spheres as difunctional and efficient electrocatalysts for overall water electrolysis, Appl. Catal. B-Environ. 204 (2017) 486–496.

[59] G.A. El-Nagar, I. Derr, A. Fetyan, C. Roth, One-pot synthesis of a high performance chitosan-nickel oxyhydroxide nanocomposite for glucose fuel cell and electro-sensing applications, Appl. Catal. B-Environ. 204 (2017) 185–199.

[60] H. Li, Y. Gong, C. Fu, H. Zhou, W. Yang, M. Guo, M. Li, Y. Kuang, A novel method to prepare a nanotubes@mesoporous carbon composite material based on waste biomass and its electrochemical performance, J. Mater. Chem. A. 5.8 (2017) 3875–3887.

[61] M. Yao, N. Wang, W. Hu, S. Komarneni, Novel hydrothermal electrodeposition to fabricate mesoporous film of Ni₀.₈Fe₀.₂ nanosheets for high performance oxygen evolution reaction, Appl. Catal. B-Environ. 233 (2018) 226–233.

[62] H.S. Min, M.G. Park, U.L. Dong, X. Wang, W. Ahn, S.H. Noh, S.M. Choi, Z.P. Cano, B. Han, Z. Chen, Bifunctionally active and durable hierarchically porous transition metal-based hybrid electrocatalyst for rechargeable metal-air batteries, Appl. Catal. B-Environ. 239 (30) (2018) 677–687.

[63] H. Li, L. Jiang, Q. Feng, Z. Huang, H. Zhou, Y. Gong, Z. Hou, W. Yang, C. Fu, Y. Kuang, Ultra-fast transfer and high storage of Li⁺/Na⁺ in MnO quantum Dots@Carbon nanotubes: appropriate quantum dots to improve the rate, Energy Storage Mater. 17 (2019) 157–166.

[64] H. Li, S. Ma, H. Cai, H. Zhou, Z. Huang, Z. Hou, J. Wu, W. Yang, H. Yi, C. Fu, Y. Kuang, Ultra-thinFe₃C nanosheets promote the adsorption and conversion of polysulfides in Lithium-Sulfur Batteries, Energy Storage Mater. 18 (2019) 338–348.

[65] H. Li, Y. Huang, H. Zhou, W. Yang, M. Li, C. Fu, Y. Kuang, One step in-situ synthesis of Co@ N, S co-doped CNTs composite with excellent HER and ORR bifunctional electrocatalytic performances, Electrochim. Acta 247 (2017) 736–744.

[66] X. Yu, M. Wang, X. Gong, Z. Guo, Z. Wang, S. Jiao, Self-supporting porous CoP-based films with phase separation structure for ultrastable overall water electrolysis at large current density, Adv. Energy Mater. 8.34 (2018) 1802445.

[67] X. Long, J. Li, S. Xiao, K. Yan, Z. Wang, H. Chen, S. Yang, A strongly coupled graphene and FeNi double hydroxide hybrid as an excellent electrocatalyst for the oxygen evolution reaction, Angew. Chem. 126.29 (2014) 7714–7718.

[68] J.W. Lee, T. Ahn, D. Soundararajan, J.M. Ko, J.D. Kim, Non-aqueous approach to the preparation of reduced graphene oxide/α-Ni(OH)₂ hybrid composites and their high capacitance behavior, Chem. Commun. 47.22 (2011) 6305–6307.

[69] M.R. Gao, X. Cao, Q. Gao, Y.F. Xu, Y.R. Zheng, J. Jiang, S.H. Yu, Nitrogen-doped graphene supported CoSe₂ nanobelt composite catalyst for efficient water oxidation, ACS Nano 8.4 (2014) 3970–3978.

[70] C. Li, B. Zhang, Y. Li, S. Hao, X. Cao, G. Yang, J. Wu, Y. Huang, Self-assembled Cu-Ni bimetal oxide 3D in-plane epitaxial structures for highly efficient oxygen evolution reaction, Appl. Catal. B-Environ. 244 (2019) 56–62.

[71] M. Kim, S. Kim, D. Song, S. Oh, K.J. Chang, E. Cho, Promotion of electrochemical oxygen evolution reaction by chemical coupling of cobalt to molybdenum carbide, Appl. Catal. B-Environ. 227 (2018) 340–348.

[72] Z. Kou, L. Zhang, Y. Ma, X. Liu, W. Zang, J. Zhang, S. Huang, Y. Du, A.K. Cheetham, J. Wang, 2D carbide nanomeshes and their assembling into 3D microflowers for efficient water splitting, Appl. Catal. B-Environ. 243 (2019) 678–685.

[73] M.B. Stevens, C.D. Trang, L.J. Enman, J. Deng, S.W. Boettcher, Reactive Fe-sites in Ni/Fe(oxy)hydroxide are responsible for exceptional oxygen electrocatalysis activity, J. Am. Chem. Soc. 139.33 (2017) 11361–11364.

[74] F. Lin, B.F. Bachman, S.W. Boettcher, Impact of electrocatalyst activity and ion permeability on water-splitting photoanodes, J. Phys. Chem. Lett. 6.13 (2015) 2427–2433.